

The Mid-Pleistocene Transition induced by delayed feedback and bistability

Courtney Quinn,^{1, a)} Jan Sieber,¹ Anna S. von der Heydt,² and Timothy M. Lenton³

¹⁾*College of Engineering, Mathematics and Physical Sciences,*

University of Exeter, Exeter EX4 4QE, United Kingdom

²⁾*Institute for Marine and Atmospheric Research, Centre for Extreme Matter and Emergent Phenomena, Utrecht University, Princetonplein 5, 3584 CC Utrecht, The Netherlands*

³⁾*Earth System Science, College of Life and Environmental Sciences, University of Exeter, Exeter EX4 4QE, United Kingdom*

(Dated: 12 June 2022)

The Mid-Pleistocene Transition, the shift from 41 kyr to 100 kyr glacial-interglacial cycles that occurred roughly 1 Myr ago, is often considered as a change in internal climate dynamics. Here we revisit the model of Quaternary climate dynamics that was proposed by Saltzman and Maasch (1988) (from this point referred to as SM88). We show that it is quantitatively similar to a scalar equation for the ice dynamics only when combining the remaining components into a single delayed feedback term. The delay is the sum of the internal times scales of ocean transport and ice sheet dynamics, which is on the order of 10 kyr.

We find that, in the absence of astronomical forcing, the delayed feedback leads to bistable behaviour, where stable large-amplitude oscillations of ice volume and an equilibrium coexist over a large range of values for the delay. We then apply astronomical forcing using the forcing data for integrated summer insolation at 65 degrees North from Huybers and Eisenman (2006). Since the precise scaling of the forcing amplitude is not known, we perform a systematic study to show how the system response depends on the forcing amplitude. We find that over a wide range of forcing amplitudes the forcing leads to a switch from small-scale oscillations of 41 kyr to large-amplitude oscillations of roughly 100 kyr without any change of other parameters. The transition in the forced model consistently occurs near the time of the Mid-Pleistocene Transition (between 1200 and 800 kyr BP) as observed in the data records from Lisiecki and Raymo (2005). This provides evidence that the MPT could have been primarily a forcing-induced switch between attractors of the internal dynamics. Small additional random disturbances make the forcing-induced transition near 800 kyr BP even more robust.

We also find that the forced system forgets its initial history during the small-scale oscillations, in particular, nearby initial conditions converge prior to transitioning. In contrast to this, in the regime of large-amplitude oscillations, the oscillation phase is very sensitive to random perturbations, which has a strong effect on the timing of the deglaciation events.

Keywords: mid-Pleistocene transition, delayed feedback, glacial dynamics, bistability

I. INTRODUCTION

The Pleistocene is characterised by its successive glacial-interglacial cycles whose documented periodicities has been a subject of interest for decades. Hays, Imbrie, and Shackleton (1976); Paillard (1998), and Ganopolski and Calov (2011) have all presented evidence

^{a)}c.quinn2@exeter.ac.uk

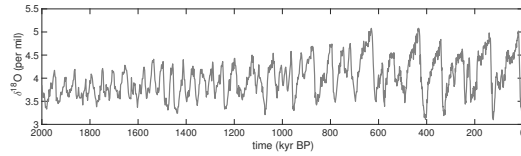


FIG. 1: Compilation of 57 globally distributed benthic $\delta^{18}\text{O}$ records for the last 2 Myr (Lisiecki and Raymo, 2005).

that orbital forcing plays a large role in the onset and termination of glacial periods, but the full extent of the variations cannot be explained solely by forcing (Ridgwell, Watson, and Raymo, 1999; Shackleton, 2000; Paillard, 2001). One actively researched aspect of the Pleistocene is the abrupt change in frequency of major glaciations known as the Mid-Pleistocene Transition (MPT) (Pisias and Moore, 1981; Maasch, 1988; Maasch and Saltzman, 1990; Paillard, 1998; Clark *et al.*, 2006; Crucifix, 2012; Ashwin and Ditlevsen, 2015). Fig. 1 shows a proxy record compiled by Lisiecki and Raymo (2005) for global temperature taken from ocean core sediments which can be directly related to global ice cover. Spectral analysis has been performed on this time series, and it has been observed that the signal of the 100-kyr cycle began to rise 1250 kyr BP and was established as the dominant cycle by 700 kyr BP (Clark *et al.*, 2006; Lisiecki and Raymo, 2007; Dijkstra, 2013). Many researchers have tried to determine not only the cause of this switch, but also the driving force behind the 100 kyr cycles themselves (Maasch and Saltzman, 1990; Saltzman and Maasch, 1991; Paillard, 1998; Gildor and Tziperman, 2001; Paillard and Parrenin, 2004; Ganopolski and Calov, 2011; Ashwin and Ditlevsen, 2015). While the 41-kyr oscillations have been attributed to external forcing (Paillard, 2001), the 100-kyr cycles have been proposed to be a result of nonlinear responses of the climate system itself (Imbrie *et al.*, 1993; Yiou *et al.*, 1994; Gildor and Tziperman, 2001).

The major glacial-interglacial cycles were originally attributed to changes in insolation due to orbital variations (i.e. the Milankovitch cycles). Milankovitch argued that summer insolation at high northern latitudes determined the main pacing of glaciations, as these changes control the length of seasons and amount of solar energy being received in high latitudes where the ice resides. The most prominent frequencies of these changes are 19 and 23 kyr due to precession and 41 kyr due to obliquity (Paillard, 2001). Precession is the orientation of the rotational axis of the earth (axial) and the rotation of the orbital axis (apsidal), and obliquity is the angle between the rotational axis and the orbital axis. Milankovitch (1941) argued that the main driving forces of climate fluctuations are obliquity and precession, which agrees with the records prior to the mid-Pleistocene transition. There is a smaller signal of orbital forcing that correlates with the 100-kyr oscillations (Imbrie *et al.*, 1993). Eccentricity, the amount the earth's orbital ellipse deviates from a circle, shifts with a main period of 413 kyr, but there are components that vary with periods between 95 kyr and 125 kyr. The amplitude of these forcing signal bands, however, are an order of magnitude smaller than the signals of the 23- and 41-kyr bands (Hays, Imbrie, and Shackleton, 1976).

Since Milankovitch's theory, there have been many other attempts to identify the cause of the MPT (see review paper by Crucifix (2012)). The starting point of our analysis are the Saltzman models of the late twentieth century. They were a collection of attempts to model the transition as a bifurcation in low-order dynamical systems due to climate feedbacks. The models typically only had three dynamic variables usually representing some measure of global ice volume, global mean temperature, and ocean circulation strength. Other modelling attempts, after the Saltzman models, include (in order of increasing complexity) threshold models (Tzedakis *et al.*, 2017), nonsmooth models (Paillard, 1998), relaxation oscillators (Ashwin and Ditlevsen, 2015), box models of intermediate complexity (Gildor and Tziperman, 2001), and Earth system models of intermediate complexity (EMICs) (Ganopolski and Calov, 2011). While all of these studies were able to reproduce a transition similar to the MPT, they are all based on the hypothesis that the MPT occurred because of some

significant change in the dynamics of the system. Huybers (2009) proposed an alternative hypothesis that the MPT was a spontaneous response to the astronomical forcing. In this study we focus on this alternative hypothesis, and provide more evidence using a previously established model by Saltzman and Maasch (1988).

The paper is arranged as follows. Section 2 revisits and analyses the three-variable Saltzman and Maasch 1988 model. We observe that two of the variables mostly act as delays in feedback loops such that we may reduce the model to a scalar equation with delayed feedback. We also identify a region of bistability at the parameter values of interest which was not explored in the original model analysis. Section 3 shows the model response in the bistable region when astronomical forcing is introduced, which includes MPT-like realisations with no change in parameters. In section 4 we investigate the sensitivity of the model. We observe that the system forgets its initial condition and has low sensitivity whenever it exhibits a small-amplitude oscillatory response. It is much more sensitive to disturbances when exhibiting a large-amplitude oscillatory response. This sensitivity affects mostly the timing of major deglaciation events. Section 5 discusses our results.

II. ADAPTATION OF THE SALTZMAN AND MAASCH MODEL

We begin by considering the original model of Saltzman and Maasch (1988), which we will refer to as SM88,

$$\dot{X}(t) = -X(t) - Y(t), \quad (1a)$$

$$\dot{Y}(t) = -pZ(t) + rY(t) + sZ(t)^2 - Z(t)^2Y(t), \quad (1b)$$

$$\dot{Z}(t) = q(-X(t) - Z(t)). \quad (1c)$$

Here X, Y, Z are scaled versions of global ice mass, atmospheric CO_2 , and North Atlantic Deep Water (NADW) respectively. More precisely, the variables represent anomalies from a background state. The first term in (1a) represents the feedbacks of global ice mass. The combined effect of damping and negative feedback from NADW production is taken to outweigh the positive feedback from ablation (melting and loss of ice through icebergs). The second term in (1a) is the direct effect of higher temperatures (caused by higher CO_2 levels) leading to loss of ice mass. In equation (1c) the negative sign of ice anomaly X is motivated by the reduction of NADW production with loss of ice mass. This equation has a time scaling q which is the ratio of ice sheet time constant (10 kyr, which equals $t = 1$ in the scaling of (1a)-(1c)) to the response time of the deep ocean. The equation for atmospheric CO_2 (1b) has a negative term $-pZ$ for the negative effect due to NADW—more NADW leads to more ventilation of the deep ocean (stronger mixing between surface and deep waters)—and an increased drawdown of atmospheric CO_2 into the deep ocean. The term rY accounts for the positive feedbacks of atmospheric CO_2 , related to changes in sea surface temperatures, sea ice extent, and sea level, which outweigh negative feedbacks. The nonlinearity $(s - Y)Z^2$ is motivated by the appearance of locally enhanced instabilities in the Southern Ocean due to increased NADW production. The NADW meets colder, denser Antarctic Bottom Water and induces vertical mixing. This brings CO_2 -rich water to the surface which releases CO_2 into the atmosphere depending on the current level of atmospheric CO_2 (Y). Each of these effects (except damping of the nonlinear terms) have an associated parameter which control their relative strengths. These were the feedbacks between global ice mass, atmospheric CO_2 , and NADW deemed most important by Saltzman and Maasch (1988). Present day studies continue to stress the interaction between these three variables as being essential for the MPT, including a study by Chalk *et al.* (2017) which uses a geochemical box model to show that carbon cycle feedbacks in the ocean circulation explain most of the variance involved in the long glacial cycles of the late Pleistocene.

A change of variable $V(t) = -X(t)$, where V is the negative of the global ice mass perturbations, replaces the two linear equations (1a) for X and (1c) for Z by a chain of linear first-order filters

$$\dot{V}(t) = Y(t) - V(t), \quad \dot{Z}(t) = q[V(t) - Z(t)]. \quad (2)$$

A linear chain of filters is well known to approximate a delay (Smith, 2010):

$$Z(t) \approx Y(t - \tau), \text{ where } \tau = 1 + \frac{1}{q}. \quad (3)$$

Appendix A gives further comments on the linear chain approximation for delays. Using this connection between linear chains and delays, we can rewrite the model as a scalar delay-differential equation (DDE) for Y . To facilitate the comparison to data at a later stage, we shift time and exploit that in the DDE the ice mass anomaly $V = -X$ is just the delayed (by time 1) CO₂ anomaly: $X(t) = -Y(t - 1)$. Thus, we may express the DDE model in terms of ice mass anomaly X :

$$\dot{X}(t) = rX(t) - pX(t - \tau) - X(t - \tau)^2[s + X(t)]. \quad (4)$$

In DDE (4) one of the parameters r, p, s, τ is redundant and could be removed by a rescaling of X and time. Thus, (4) is objectively simpler than the original SM88 model (1) as it has fewer free parameters. For the purpose of model comparison, the DDE system will be left as above.

A. Dynamics of DDE, compared to SM88

We initially perform a systematic analysis of DDE (4) and compare it to the original SM88. We find that models (1) and (4) have the same long-time behaviour (using the relation $q = \frac{1}{\tau-1}$ implied by (3)).

Since delays, whether in the form of chains as in SM88 or explicit, don't affect location of equilibria, i.e. $X(t) = X(t - \tau)$ (or $X(t) = -Y(t) = -Z(t)$), equilibria for both models, (1) and (4), (called $X_{\text{eq},j}$) satisfy

$$0 = -pX_{\text{eq}} + rX_{\text{eq}} - sX_{\text{eq}}^2 - X_{\text{eq}}^3. \quad (5)$$

Thus, we have a trivial equilibrium $X_{\text{eq},1} = 0$ for all parameter values and non-zero equilibria $X_{\text{eq},2,3}$ for $s^2 > 4(p - r)$:

$$X_{\text{eq}_{2,3}} = \frac{1}{2} \left[-s \pm \sqrt{s^2 - 4(p - r)} \right]. \quad (6)$$

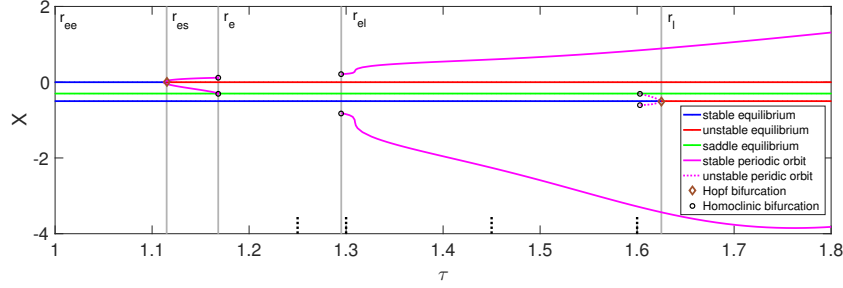
The stability of the equilibria may differ, however, since eigenvalues of the linearisation may cross the imaginary axis (leading to oscillations in a Hopf bifurcation (Kuznetsov, 2013)) at different parameter values for (1) and (4).

All other trajectories have to be studied numerically (for both, SM88 (1) and DDE(4)). Since the scaling between the two models are the exactly same, we will use values for p, r , and s from Saltzman and Maasch (1988) for all numerical studies:

$$p = 0.95, \quad r = 0.8, \quad s = 0.8, \quad (7)$$

while varying the timescale (or delay) of the feedback processes (τ for DDE (4), q for SM88 model (1)). A value of $q = 1.2$ was used in SM88, which would correspond to $\tau \approx 1.83$. The only constraint on q was $q \geq 1$ (q was defined as the ratio of ice sheet time constant, 10 kyr, to the slow response time of deep ocean). The value of q by Saltzman and Maasch (1988) would approximate a deep ocean response time of around 8.3 kyr. This is long for ocean timescales, so values below this would be just as physically relevant. This would put realistic values of τ in the range [1,2].

Figure 2 shows the bifurcation diagrams for varying τ in DDE (4) and SM88 model (1), respectively. Although the locations of bifurcations are slightly shifted, qualitatively the two figures agree nicely. In particular, even though the space of possible initial conditions for DDE (4) is infinite-dimensional (every possible history on $[-\tau, 0]$ gives a different trajectory), the long-time behaviour of trajectories in the $(X(t), X(t - \tau))$ -plane follows a two-dimensional ODE in the range we explored. The diagrams in Fig. 2 are partitioned into five main regions of different global behaviour separated by grey vertical lines can be seen in both figures. From left to right the attractors in each region are:



(a) DDE model (4)

The dotted black lines indicate values of τ used in section III: $\tau_{\text{ref}} = 1.25$, $\tau_1 = 1.3$, $\tau_2 = 1.45$, $\tau_3 = 1.6$.

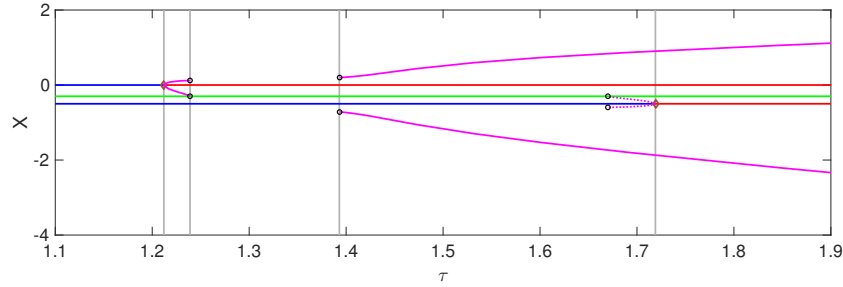
(b) SM88 ($\tau = \frac{1}{q} + 1$)

FIG. 2: Bifurcation diagrams of both models for delay parameter τ . Other parameters: $p = 0.95$, $r = 0.8$, $s = 0.8$.

- $[r_{ee}]$ two stable equilibria,
- $[r_{es}]$ one stable equilibrium and one stable small-amplitude period solution,
- $[r_e]$ one stable equilibrium,
- $[r_{el}]$ one stable equilibrium and one stable large-amplitude periodic solution, and
- $[r_l]$ one stable large-amplitude periodic solution.

The region of interest in this study is the bistable region with large-amplitude periodic orbits $[r_{el}]$. Note that $[r_{el}]$ can be split further into two sections: one containing unstable periodic orbits and the other not. The effect of the unstable periodic orbits is a drastically reduced basin of attraction for the stable equilibrium. However, since there is no change in the attractors, we will consider these as one region. Region $[r_{el}]$ was not discussed in a later parameter study of the original model Maasch and Saltzman (1990). For the remainder of this paper we will discuss only the DDE model, but similar results can be seen for the ODE model.

B. The bistable region $[r_{el}]$

The focus of this study is the bistability seen for $\tau \in [1.295, 1.625]$ in the DDE system. In this region there are two possible stable solutions (shown in Fig. 3): a stable equilibrium and stable large amplitude periodic orbits. The time profile of the periodic orbits has the asymmetrical shape observed in the ice age cycles of the late Pleistocene. The asymmetry is attributed to a slow accumulation of ice mass followed by rapid melting. In addition, the period remains between 109 and 120 kyr throughout the bistable region (with an exception of τ very close to the $[r_e-r_{el}]$ boundary where the period approaches infinity). This cycle length agrees with what is seen in the data (even more so when one adds the external forcing; see Sec. III). In previous studies of SM88 model (1), a transition between two stable states was enforced by a parameter shift through a Hopf bifurcation (Saltzman and

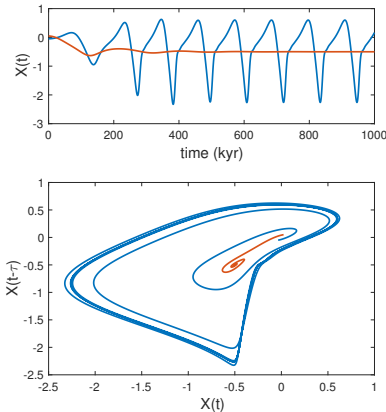


FIG. 3: Example trajectories in the bistable region $[r_{el}]$ for $\tau = 1.45$; $X(t) = -0.05$ (blue) and $X(t) = 0.05$ (red) for $t < 0$. Top- time profiles, bottom - phase portraits.

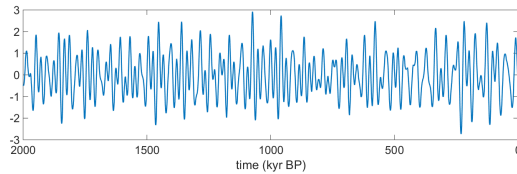


FIG. 4: Normalised integrated July insolation at 65°N , adapted from Huybers and Eisenman (2006).

Maasch, 1988; Maasch and Saltzman, 1990). We will demonstrate in the next section that the bistability in region $[r_{el}]$ makes transitions between the two states possible without any change of parameter when the model is subjected to external forcing.

III. THE MID-PLEISTOCENE TRANSITION UNDER THE FORCED MODEL

In this section we show that when adding astronomical forcing to model (4), a transition typically occurs at the same time as the MPT is seen in recorded data without further parameter tuning. In section III A we describe the astronomical forcing considered and how we include it in the model. We then examine the responses for different delays and different forcing strengths in sections III B and III C.

A. Astronomical forcing

Hays, Imbrie, and Shackleton (1976) have provided evidence that the glacial cycles during the Pleistocene are driven primarily by variations in the earth's orbital cycle. This includes changes in precession (orientation of the rotational axis), obliquity (angle between the rotational axis and orbital axis), and eccentricity (orbital ellipse's deviation from a circle). These modes vary approximately periodically, with cycle lengths of 19/23 kyr, 41 kyr, and 100 kyr respectively (Milankovitch, 1941; Berger, 1978; Huybers and Eisenman, 2006). Fig. 4 shows a time series of summer insolation at 65°N computed by Huybers and Eisenman (2006) based on the model introduced by Huybers (2006). To investigate the effect of this forcing on DDE (4), we include the astronomical forcing in the same way as Maasch and Saltzman (1990). We add forcing signal $M(t)$ shown in Fig. 4 with negative amplitude

u ,

$$\dot{X}(t) = rX(t) - pX(t - \tau) - X(t - \tau)^2[s + X(t)] - uM(t). \quad (8)$$

We are interested in how the bistable region responds to this external forcing in dependence of two parameters: the delay τ and the forcing amplitude u .

For small u the system is expected to exhibit two types of responses to forcing in the bistable region. Each of them is a perturbation of an attractor of the unforced system, namely the equilibrium and the large-amplitude periodic orbit, which persist for small u . We will refer to these responses as the *small-amplitude* and the *large-amplitude* response (compare red and blue time profiles in Fig. 5c). For increasing u we expect to observe increasingly frequent transitions between these responses. For large forcing amplitudes u the internal dynamics of the model will be dominated by the forcing.

B. Responses for different delays in the bistable region

We choose a moderate value of the forcing amplitude $u = 0.25$ and investigate the response at four values of τ , labelled in Fig. 2a by τ_{ref} , τ_1 , τ_2 , and τ_3 . The first value $\tau_{\text{ref}} = 1.25$ is outside of the region of bistability and is used as a reference trajectory to which the solution trajectories for the other delays τ_1 , τ_2 and τ_3 are compared. The results are shown in Fig. 5 (response for τ_{ref} shown in red, for other delays in blue)

The first comparison is made close to the boundary $[r_e]-[r_{ei}]$ at $\tau_1 = 1.3$. We see in figure 5a that both trajectories change in synchrony, exhibiting only the small-amplitude response. In the middle of the bistable region ($\tau_2 = 1.45$, shown in Fig. 5b), the solution shows a small-amplitude response in most of the first half of the time window and a large-amplitude response in the second half. Close to the Hopf bifurcation of the autonomous stable equilibrium ($\tau_3 = 1.6$, shown in Fig. 5c) the solution exhibits primarily a large-amplitude response. This is expected due to the weakening attraction of the autonomous stable equilibrium and its shrinking basin of attraction. We will demonstrate in the following section that these transitions generate dynamics with time profiles that are qualitatively similar to the records of the MPT.

C. Variable forcing strength

For the exploration of the effect of different forcing strengths, we take the same values for τ as in Fig. 5, covering the range of the bistable region. For each τ we compute trajectories for different u , ranging from $u = 0$ to $u = 0.6$. Figure 6 shows the difference of these trajectories to a respective reference trajectory for $\tau_{\text{ref}} = 1.25$ and the same initial condition and forcing strength u , averaged over a window of length τ . We note that differences to a reference trajectory at $u = 0$ and identical delay τ (using same initial condition) give qualitatively similar results.

Remarkably, figures 6a and 6b show that there is a distinct period around 700-800 kyr BP where the solutions diverge from the reference trajectory in a large range of forcing strengths u . This suggests that some aspect of the forcing around this time kicks the trajectories into the basin of attraction of the large-amplitude response. An additional area like this is seen in figure 6b near 1600 kyr BP.

The second interesting feature in all three figures is a threshold behaviour with respect to the forcing strength u : below a certain value of u specific to each τ , transitions do not occur such that the solutions just track the reference trajectory. Above this value trajectories suddenly can make this transition.

While the starting time of the large-amplitude response areas in figures 6a and 6b is specific to the forcing profile by Huybers and Eisenman (2006) in Fig. 4, the threshold with respect to u is also present when harmonic forcing is added, for example, of the form

$$M(t) = -\sin\left(\frac{2\pi}{4.1}t\right). \quad (9)$$

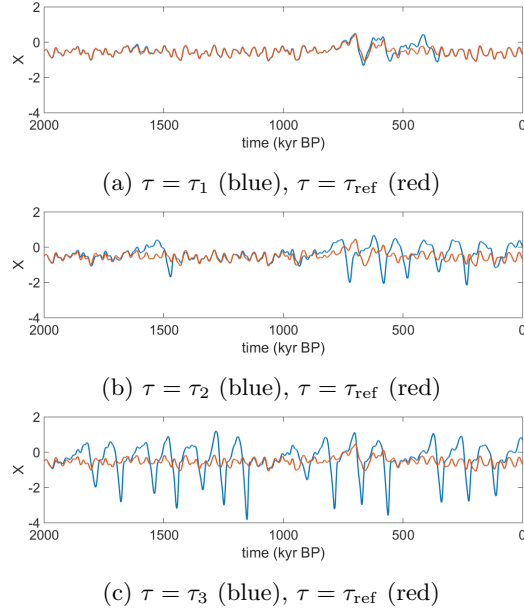


FIG. 5: Trajectories in bistable region (blue) compared to a reference trajectory at $\tau_{\text{ref}} = 1.25$ (red) for delays (a) $\tau_1 = 1.30$, close to homoclinic connection, (b) $\tau_2 = 1.45$, middle of bistable region, and (c) $\tau_3 = 1.60$, close to Hopf bifurcation. Values of τ are indicated on bifurcation diagram in Fig. 2a. Other parameters: $p = 0.95$, $r = 0.8$, $s = 0.8$, and $u = 0.25$. Initial condition $X(t) = -0.5$ for $t < 0$ in all cases.

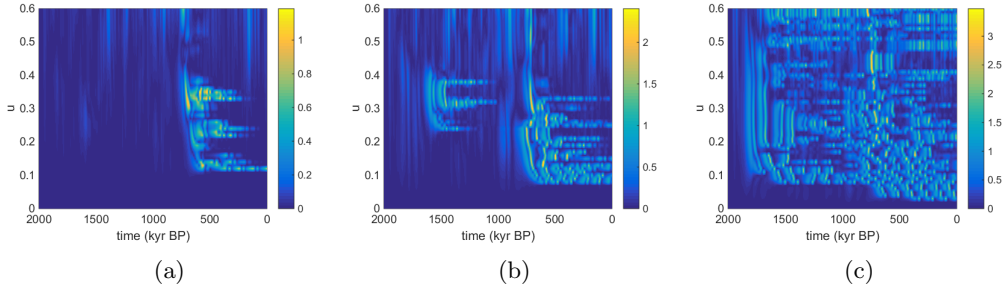


FIG. 6: Distance from reference solution at $\tau_{\text{ref}} = 1.25$, for different forcing strengths u . Averages taken over window length of size τ . (a) $\tau = 1.30$, close to homoclinic connection. (b) $\tau = 1.45$, middle of bistable region. (c) $\tau = 1.60$, close to Hopf bifurcation. Initial condition $X(t) = -0.5$ for $t < 0$ in all cases.

This forcing has a period of 41 kyr. If $u > 0$, equation (8) also has two possible responses: a small-amplitude nearly sinusoidal signal with a 41 kyr period, or a large-amplitude asymmetrical quasiperiodic response. With this periodic forcing but parameters otherwise identical to those in Fig. 6b, we observe a transition from small amplitude to large amplitude response at $u = 0.08$. We can show that this transition is due to changing basins of attraction for the small amplitude response.

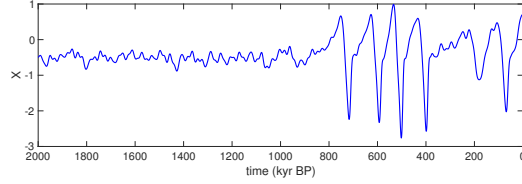


FIG. 7: Example trajectory that exhibits an MPT-like transition with $\tau = 1.45$ and $u = 0.15$.

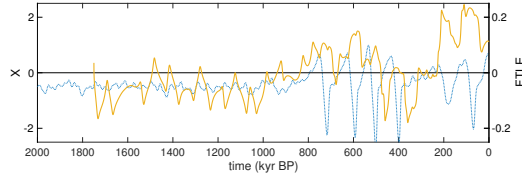


FIG. 8: Finite-time Lyapunov exponents for window length $w = 250$ kyr computed from model run with $\tau = 1.45$ and $u = 0.15$: $X(t)$ (dotted blue), $\text{FTLE}([t - w, t])$ (gold).

IV. MODEL SENSITIVITY TO NOISE: DESYNCHRONISATION AND INCREASED ROBUSTNESS OF TRANSITION

A. Finite-time Lyapunov Exponents

To analyse how trajectories depend on their history at specific instances of the forcing, we compute finite-time Lyapunov exponents (FTLEs) using a QR decomposition method (details in Appendix B). This method was previously used in De Saedeleer, Crucifix, and Wiczepek (2013) to illustrate the desynchronisation of nearby trajectories in a van der Pol-type oscillator model. We will apply the ideas presented in that study to our forced model.

The difference between FTLEs and classical Lyapunov exponents is that FTLEs are recorded for a family of time windows of finite length w rather than over the entire long time run. Thus, FTLEs are time-dependent functions instead of real numbers. A positive FTLE along a given trajectory $X(t)$ at time t_0 indicates that some nearby trajectories diverge exponentially from $X(t)$ in the time window $[t_0 - w, t_0]$. Therefore, $X(t)$ is sensitive to small perturbations in the time window $[t_0 - w, t_0]$. While a trajectory could be asymptotically stable, a positive FTLE at a time t_0 indicates temporary amplification of perturbations from the attracting trajectory (observed as temporary desynchronisation, see (De Saedeleer, Crucifix, and Wiczepek, 2013)).

B. FTLE implications on MPT and timing of major deglaciations

We analyse one trajectory, showing a forcing-induced MPT ($\tau = 1.45$, $u = 0.15$, shown in Fig. 7). We compute the FTLE over a sliding window of our example MPT trajectory with a window length of $w = 250$ kyr. This window length is chosen in order to filter out the dominant frequencies of the forcing. Similar results are seen with any window lengths w from 150-500 kyr.

Fig. 8 shows the time profile of the largest FTLE along the trajectory. Before the transition around 800 kyr BP, the FTLE generally remains negative apart from a few short excursions above zero. At 1000 kyr BP the FTLE approaches zero and remains there for some time. Just before 800 kyr BP it becomes positive and then on average stays positive for the remainder of the trajectory.

The negative FTLEs leading up to the transition confirm that the trajectory forgets

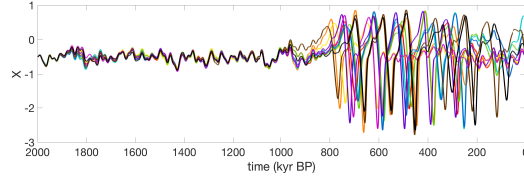


FIG. 9: Trajectories of DDE model with noise: $u = 0.15$, $\sigma = 0.005$, $\tau = 1.45$.

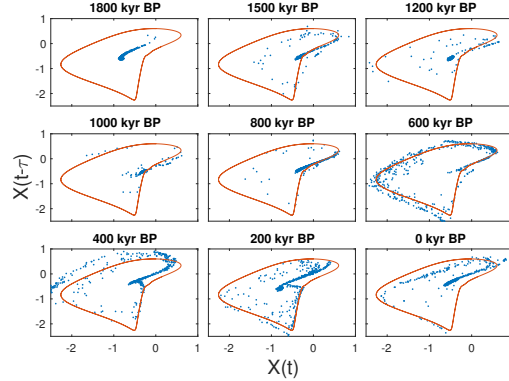


FIG. 10: Phase portraits at specific time instances of 500 model runs with noise: $u = 0.15$, $\sigma = 0.005$, $\tau = 1.45$. The red curve represents the unforced periodic orbit.

its initial history and the effect of past disturbances. In particular, this implies that the infinite-dimensional nature of the DDE's possible initial conditions does not play a role for the MPT. Whenever the system is exhibiting the small-amplitude response we observed negative FTLEs.

The positive FTLEs indicate a sensitivity of the trajectory during the large-amplitude response. This sensitivity affects the precise timing of the deglaciations, as we now demonstrate by noise-induced desynchronisation of nearby trajectories.

To explore further the desynchronisation phenomenon outlined in De Saedeleer, Crucifix, and Wiczorek (2013), we add noise to our system. The stochastic delay differential equation (SDDE) is then given as

$$dX(t) = [-pX(t - \tau) + rX(t) - sX(t - \tau)^2 - X(t - \tau)^2 X(t) - uM(t)]dt + \sigma dW(t), \quad (10)$$

Here, $W(t)$ is standard white noise and σ is the noise amplitude. We will always consider σ as a fraction of the forcing amplitude u , i.e. $\sigma = \frac{u}{30}$.

We set the deterministic forcing strength $u = 0.15$ and the noise amplitude $\sigma = 0.005$. We ran 500 realisations of the model, all with the same initial history. The results of 10 randomly selected realisations can be seen in Fig. 9. Up until 1000 kyr BP all trajectories generally track the same solution with only minor short desynchronisations. Shortly after 1000 kyr BP the trajectories begin to diverge, making the transition to the large amplitude oscillation state at different times. The trajectories then stay desynchronised, which corresponds to being at a different phase along the large amplitude oscillation. We illustrate this phenomenon in Fig. 10, where we show the distribution of trajectories in the $(X(t), X(t - \tau))$ -plane along the unforced periodic orbit. Figure 11 shows the transition from synchronization to desynchronization in a density plot. At approximately 800 kyr BP (indicated by the gray line) the probability density makes a sharp transition from a small-variance to a large-variance-low-maximum density. The timing of this transition agrees with the first large positive excursion of the FTLE in the deterministic case and with the MPT. The standard deviation shows this transition as well, but with a lag of about 50 kyr.

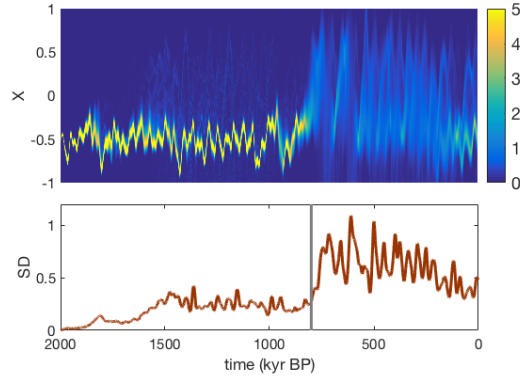


FIG. 11: Probability density in time (top) and its standard deviation (bottom) of 500 model runs with noise: $u = 0.15$, $\sigma = 0.005$, $\tau = 1.45$. The gray line indicates 800 kyr BP

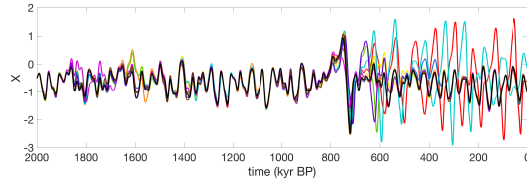


FIG. 12: Trajectories of DDE model with noise: $u = 0.45$, $\sigma = 0.015$, $\tau = 1.45$.

C. Effect of noise with stronger forcing

Figure 12 shows that the addition of noise enhances the MPT for strong forcing. When adding noise, we observe transitions for forcing strengths u for which there was no transition in the deterministic case (compare Figures 6b and 13). In Fig. 6b the last persistent transition occurs at $u = 0.33$. Fixing the forcing strength at $u = 0.45$, we compute ten realisations. Here, two realisations exhibit transitions that persist until the end of the run. Although the transitions don't appear as commonly as in the weaker forcing case, with noise it is possible to observe an MPT-like transition across a wider range of forcing amplitudes.

Figure 13 shows a systematic overview of the transition enhancing effect of noise. We added noise of amplitude $\sigma = \frac{u}{30}$ and compute the distance diagram as in Fig 6b. We observe transitions occurring above the maximal value of u for which transitions occurred in the deterministic case.

V. DISCUSSION

We have presented an analysis of the well known Saltzman and Maasch (1988) model of Quaternary climate dynamics. We have shown that it can be reduced to a scalar equation for the ice mass anomaly $X(t)$, by collecting all other variables into a delayed feedback term. Through this formulation we are able to explore the dependence on the time scale τ of the delay in this feedback. We discovered a region in which a stable equilibrium and stable large-amplitude periodic orbit coexist for the unforced system.

We observe two different responses to astronomical forcing of the type proposed by Huybers and Eisenman (2006): small-amplitude response (tracking the equilibrium) and large-amplitude response (tracking the periodic orbit). In the deterministic bistable region the model exhibits a switching behaviour between these two responses. The timings of the switches are robust for different values of the delay and forcing strength. The most promi-

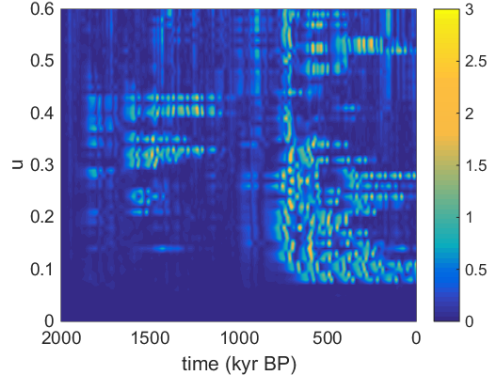


FIG. 13: Same as Fig 6b except with noise: $\sigma = \frac{u}{30}$, $\tau = 1.45$.

ment switch occurs around 800 kyr BP which is within the range of when the Mid-Pleistocene Transition is believed to have occurred.

One trajectory showing the MPT is analysed using finite-time Lyapunov exponents. Using a window of 250 kyr we observe that the largest FTLE is negative up to 1000 kyr BP, remains around zero during the transition, and is mostly positive after the transition. We demonstrate that this positivity induces phase desynchronisation which is then confirmed by adding noise to the model. The added noise also allows for the transition to be seen with stronger forcing.

The novelty of this study is in the observation that transitions similar to the MPT occur robustly without any change in parameter. The transition arises from the interplay between astronomical forcing and bistability rather than a shift of a system parameter through a bifurcation. We also highlight that with noise the transition is possible but doesn't always occur, and that the phase (or timings of the deglaciations) are highly variable. While our demonstration was done for the specific low-order model SM88, we conjecture many of the effects (instability caused by delayed feedback, transition induced but not solely caused by the forcing) to be present in other models with similar bistability.

Some questions that arise from this study will need to be addressed by deeper mathematical analysis. Why does the model prefer certain times to switch, and what causes the sharp threshold in forcing strength where switching becomes possible, visible in Fig. 6? The latter can be answered by studying the simple harmonic forcing (9) with the dominant period of 41 kyr, seen in the astronomical forcing, in more detail. We also note that these results seen are due to one specific astronomical forcing time series (65°N summer integrated insolation). Future work should consider other forcing time series to assess the robustness of this phenomenon.

Appendix A: The linear chain approximation

A linear chain of first-order ODEs approximates a delay in the following sense (see Smith (2010) for a precise derivation). We focus on the case of scalar ODEs here, but this derivation is also valid for vectors \vec{y}_0 . Consider a system of $n + 1$ ODEs of the form

$$\frac{dy_0}{dt} = F(y_0(t), y_N(t)), \quad (\text{A1a})$$

$$\frac{dy_i}{dt} = a(y_{i-1}(t) - y_i(t)) \quad i = 1, \dots, N. \quad (\text{A1b})$$

Extracting system (A1b) we have

$$\frac{d\vec{y}}{dt} = A\vec{y}(t) + \vec{b}(t), \quad (\text{A2})$$

where A is an $N \times N$ matrix of the form

$$A = \begin{bmatrix} -a & 0 & \dots & \dots & 0 \\ a & -a & \ddots & & \vdots \\ 0 & a & -a & \ddots & \vdots \\ \vdots & \ddots & \ddots & \ddots & 0 \\ 0 & \dots & 0 & a & -a \end{bmatrix} \quad (\text{A3})$$

and $\vec{y}(t), \vec{b}(t)$ are $N \times 1$ vectors of the form

$$\vec{y}(t) = \begin{bmatrix} y_1(t) \\ y_2(t) \\ \vdots \\ y_N(t) \end{bmatrix} \quad \vec{b}(t) = \begin{bmatrix} ay_0(t) \\ 0 \\ \vdots \\ 0 \end{bmatrix} \quad (\text{A4})$$

Since A is non-diagonalisable, the fundamental solution matrix of (A2) is given by

$$\Phi(t) = Pe^{-at}e^{Gt}P^{-1} \quad (\text{A5})$$

where $G = P^{-1}AP + aI$, and P is a matrix of generalised eigenvectors. (See Perko (2013) for a detailed derivation.) In our case P is a rotation matrix

$$P = \begin{bmatrix} 0 & \dots & 0 & 1 \\ \vdots & & \ddots & 0 \\ 0 & \ddots & & \vdots \\ 1 & 0 & \dots & 0 \end{bmatrix}, \quad (\text{A6})$$

and $P^{-1} = P$. Computing the last exponential term in (A5),

$$e^{Gt} = \begin{bmatrix} 1 & at & \frac{a^2t^2}{2!} & \dots & \frac{a^{N-2}t^{N-2}}{(N-2)!} & \frac{a^{N-1}t^{N-1}}{(N-1)!} \\ 0 & 1 & at & \dots & \frac{a^{N-3}t^{N-3}}{(N-3)!} & \frac{a^{N-2}t^{N-2}}{(N-2)!} \\ \vdots & \ddots & 1 & \ddots & \vdots & \vdots \\ \vdots & & \ddots & \ddots & at & \frac{a^3t^2}{2!} \\ \vdots & & & \ddots & 1 & at \\ 0 & \dots & \dots & \dots & 0 & 1 \end{bmatrix}. \quad (\text{A7})$$

From Perko (2013) we know the fundamental solution can be expressed as

$$\vec{y}(t) = \Phi(t)\vec{y}(0) + \int_0^t \Phi(t)\Phi^{-1}(s)\vec{b}(s)ds. \quad (\text{A8})$$

In our system this simplifies to

$$\vec{y}(t) = \Phi(t)\vec{y}(0) + \int_0^t e^{-a(t-s)}y_0(s)\vec{\Psi}(t-s)ds. \quad (\text{A9})$$

where

$$\vec{\Psi}(t-s) = \begin{bmatrix} a \\ a^2(t-s) \\ \frac{a^3(t-s)^2}{2!} \\ \vdots \\ \frac{a^{N-1}(t-s)^{N-2}}{(N-2)!} \\ \frac{a^N(t-s)^{N-1}}{(N-1)!} \end{bmatrix}. \quad (\text{A10})$$

Extending the integral in (A9) back to $-\infty$ we lose the dependence on the initial condition,

$$\vec{y}(t) = \int_{-\infty}^t e^{-a(t-s)} y_0(s) \vec{\Psi}(t-s) ds. \quad (\text{A11})$$

Looking at the N th component of (A11) and using the change of variables $\tau = t - s$, we obtain

$$y_N(t) = \int_0^\infty y_0(t-\tau) \frac{a^N \tau^{N-1}}{(N-1)!} e^{-a\tau} d\tau. \quad (\text{A12})$$

As $N \rightarrow \infty$ and $a \sim N/\tau$, the kernel of (A12) approaches a delta function at τ . This allows us to approximate (A1a) as

$$\frac{dy_0}{dt} = F(y_0(t), y_0(t-\tau)). \quad (\text{A13})$$

Appendix B: Computation of Finite-Time Lyapunov Exponents (FTLEs)

Our algorithm for computing Lyapunov exponents for a delay differential equation (DDE) follows from Farmer (1982).

a. Linearisation We consider a trajectory $X(t)$ of (8) and linearize (8) along this trajectory:

$$\dot{x}(t) = J_0(t)x(t) + J_\tau(t)x(t-\tau), \quad (\text{B1})$$

where J_0 and J_τ are the derivatives of the right-hand side of (8) with respect to $X(t)$ and $X(t-\tau)$:

$$J_0(t) = r - X(t-\tau)^2, \quad (\text{B2})$$

$$J_\tau(t) = -p - 2sX(t-\tau) - 2X(t)X(t-\tau). \quad (\text{B3})$$

b. Discretisation We consider an approximate solution of (B1) $x_i = x(t_i)$ for $t_i = t_0 + ih$, where h is a small step size, obtained using a second order trapezoidal numerical solver for DDEs. We then discretize (B1) into $m = \tau/h$ steps,

$$\vec{y}_{i+1} = M_i \vec{y}_i; \quad \vec{y}_i = [x_i, \dots, x_{i-m}]^T, \quad (\text{B4})$$

where M_i is a square $(m+1) \times (m+1)$ matrix of the form

$$M_i = \begin{bmatrix} M_{i,1} & 0 & \dots & M_{i,m} & M_{i,m+1} \\ 1 & 0 & \dots & 0 & 0 \\ 0 & \ddots & & \vdots & \vdots \\ \vdots & & \ddots & 0 & \vdots \\ 0 & \dots & 0 & 1 & 0 \end{bmatrix}$$

with entries

$$\begin{aligned} M_{i,1} &= 1 + \frac{h}{2}(J_0(t_{i+1}) + J_0(t_i)) + \frac{h^2}{2}J_0(t_{i+1})J_0(t_i), \\ M_{i,m} &= \frac{h}{2}J_\tau(t_{i+1}), \\ M_{i,m+1} &= \frac{h}{2}J_\tau(t_i) + \frac{h^2}{2}J_0(t_{i+1})J_\tau(t_i). \end{aligned}$$

c. QR method We use a continuous QR algorithm for computing the Lyapunov exponents (see Dieci, Russell, and Van Vleck (1997)). Although DDEs have an infinite number of Lyapunov exponents, this method allows us to compute up to $m + 1$ through the discretisation. We can choose to compute only the largest ℓ Lyapunov exponents by using a non-square Q . We initialise an arbitrary orthogonal Q_0 as an $m \times \ell$ matrix of form

$$Q_0 = \begin{bmatrix} I_\ell \\ 0_{(m-\ell) \times \ell} \end{bmatrix}.$$

Note that I_ℓ is the $\ell \times \ell$ identity matrix and $0_{(m-\ell) \times \ell}$ is an $(m - \ell) \times \ell$ zero matrix. We define iteratively Q_i and R_i by the QR decomposition of $M_i Q_{i-1}$ (matlab command `qr(M_i Q_{i-1}, 0)`),

$$Q_i R_i = M_i Q_{i-1}, \quad (\text{B5})$$

which produces a square $\ell \times \ell$ upper triangular matrix R_i with diagonal entries $R_{i,jj} > 0$ ($j = 1, \dots, \ell$). We store R_i for each timestep. After N timesteps we have the relation

$$Q_N R_N \dots R_1 = M_N \dots M_1 Q_0. \quad (\text{B6})$$

The infinite Lyapunov exponents can then be approximated by

$$\lambda_j = \frac{1}{N} \sum_{i=0}^N \ln R_{i,jj}. \quad (\text{B7})$$

For FTLEs we truncate the above sum after $W = w/h$ timesteps to obtain a time series, i.e.

$$\lambda_{j,n} = \frac{1}{hW} \sum_{i=n-W}^n \ln R_{i,jj}, \quad (\text{B8})$$

where w is the desired time window length and n starts at step W .

ACKNOWLEDGMENTS

C.Q., J.S and T.L. have received funding from the European Union’s Horizon 2020 research and innovation programme under the Marie Skłodowska-Curie grant agreement No 643073. J.S. gratefully acknowledges the financial support of the EPSRC via grants EP/N023544/1 and EP/N014391/1.

- Ashwin, P. and Ditlevsen, P., “The middle pleistocene transition as a generic bifurcation on a slow manifold,” *Climate Dynamics* **45**, 2683–2695 (2015).
- Berger, A. L., “Long-term variations of daily insolation and quaternary climatic changes,” *Journal of the atmospheric sciences* **35**, 2362–2367 (1978).
- Chalk, T. B., Hain, M. P., Foster, G. L., Rohling, E. J., Sexton, P. F., Badger, M. P., Cherry, S. G., Hasenfratz, A. P., Haug, G. H., Jaccard, S. L., *et al.*, “Causes of ice age intensification across the mid-pleistocene transition,” *Proceedings of the National Academy of Sciences* **114**, 13114–13119 (2017).
- Clark, P. U., Archer, D., Pollard, D., Blum, J. D., Rial, J. A., Brovkin, V., Mix, A. C., Pisias, N. G., and Roy, M., “The middle pleistocene transition: characteristics, mechanisms, and implications for long-term changes in atmospheric p_{CO_2} ,” *Quaternary Science Reviews* **25**, 3150–3184 (2006).
- Crucifix, M., “Oscillators and relaxation phenomena in pleistocene climate theory,” *Phil. Trans. R. Soc. A* **370**, 1140–1165 (2012).
- De Saedeleer, B., Crucifix, M., and Wiczeorek, S., “Is the astronomical forcing a reliable and unique pacemaker for climate? a conceptual model study,” *Climate Dynamics* **40**, 273–294 (2013).
- Dieci, L., Russell, R. D., and Van Vleck, E. S., “On the computation of lyapunov exponents for continuous dynamical systems,” *SIAM journal on numerical analysis* **34**, 402–423 (1997).
- Dijkstra, H. A., *Nonlinear climate dynamics* (Cambridge University Press, 2013).
- Farmer, J. D., “Chaotic attractors of an infinite-dimensional dynamical system,” *Physica D: Nonlinear Phenomena* **4**, 366–393 (1982).
- Ganopolski, A. and Calov, R., “The role of orbital forcing, carbon dioxide and regolith in 100 kyr glacial cycles,” *Climate of the Past* **7**, 1415–1425 (2011).

- Gildor, H. and Tziperman, E., "A sea ice climate switch mechanism for the 100-kyr glacial cycles," *Journal of Geophysical Research: Oceans* **106**, 9117–9133 (2001).
- Hays, J. D., Imbrie, J., and Shackleton, N. J., "Variations in the earth's orbit: pacemaker of the ice ages," *Science* **194**, 1121–1132 (1976).
- Huybers, P., "Early pleistocene glacial cycles and the integrated summer insolation forcing," *Science* **313**, 508–511 (2006).
- Huybers, P., "Pleistocene glacial variability as a chaotic response to obliquity forcing," *Climate of the Past* **5**, 481–488 (2009).
- Huybers, P. and Eisenman, I., "Integrated summer insolation calculations. noaa/ncdc paleoclimatology program data contribution# 2006-079," (2006).
- Imbrie, J., Berger, A., Boyle, E., Clemens, S., Duffy, A., Howard, W., Kukla, G., Kutzbach, J., Martinson, D., McIntyre, A., *et al.*, "On the structure and origin of major glaciation cycles 2. the 100,000-year cycle," *Paleoceanography* **8**, 699–735 (1993).
- Kuznetsov, Y. A., *Elements of applied bifurcation theory*, Vol. 112 (Springer Science & Business Media, 2013).
- Lisiecki, L. E. and Raymo, M. E., "A pliocene-pleistocene stack of 57 globally distributed benthic $\delta^{18}\text{O}$ records," *Paleoceanography* **20** (2005).
- Lisiecki, L. E. and Raymo, M. E., "Plio-pleistocene climate evolution: trends and transitions in glacial cycle dynamics," *Quaternary Science Reviews* **26**, 56–69 (2007).
- Maasch, K., "Statistical detection of the mid-pleistocene transition," *Climate dynamics* **2**, 133–143 (1988).
- Maasch, K. A. and Saltzman, B., "A low-order dynamical model of global climatic variability over the full pleistocene," *Journal of Geophysical Research: Atmospheres* **95**, 1955–1963 (1990).
- Milankovitch, M., "History of radiation on the earth and its use for the problem of the ice ages," *K. Serb. Akad. Beogr* (1941).
- Paillard, D., "The timing of pleistocene glaciations from a simple multiple-state climate model," *Nature* **391**, 378–381 (1998).
- Paillard, D., "Glacial cycles: toward a new paradigm," *Reviews of Geophysics* **39**, 325–346 (2001).
- Paillard, D. and Parrenin, F., "The antarctic ice sheet and the triggering of deglaciations," *Earth and Planetary Science Letters* **227**, 263–271 (2004).
- Perko, L., *Differential equations and dynamical systems*, Vol. 7 (Springer Science & Business Media, 2013).
- Pisias, N. G. and Moore, T., "The evolution of pleistocene climate: a time series approach," *Earth and Planetary Science Letters* **52**, 450–458 (1981).
- Ridgwell, A. J., Watson, A. J., and Raymo, M. E., "Is the spectral signature of the 100 kyr glacial cycle consistent with a milankovitch origin?" *Paleoceanography* **14**, 437–440 (1999).
- Saltzman, B. and Maasch, K. A., "Carbon cycle instability as a cause of the late pleistocene ice age oscillations: modeling the asymmetric response," *Global biogeochemical cycles* **2**, 177–185 (1988).
- Saltzman, B. and Maasch, K. A., "A first-order global model of late cenozoic climatic change ii. further analysis based on a simplification of CO_2 dynamics," *Climate Dynamics* **5**, 201–210 (1991).
- Shackleton, N. J., "The 100,000-year ice-age cycle identified and found to lag temperature, carbon dioxide, and orbital eccentricity," *Science* **289**, 1897–1902 (2000).
- Smith, H., *An introduction to delay differential equations with applications to the life sciences*, Vol. 57 (Springer Science & Business Media, 2010).
- Tzedakis, P., Crucifix, M., Mitsui, T., and Wolff, E. W., "A simple rule to determine which insolation cycles lead to interglacials," *Nature* **542**, 427–432 (2017).
- Yiou, P., Ghil, M., Jouzel, J., Paillard, D., and Vautard, R., "Nonlinear variability of the climatic system from singular and power spectra of late quaternary records," *Climate Dynamics* **9**, 371–389 (1994).